Vacuum ultraviolet excitation spectra of lanthanide-doped hexafluoroelpasolites

Peter A Tanner[1], **Chang-Kui Duan**[1,2], **Vladimir N Makhov**[3],
Marco Kirm[4] **and Nicolas M Khaidukov**[5]

[1] Department of Biology and Chemistry, City University of Hong Kong, Tat Chee Avenue,
Kowloon, Hong Kong SAR, People's Republic of China
[2] Institute of Modern Physics, Chongqing University of Post and Telecommunications,
Chongqing 400065, People's Republic of China
[3] P N Lebedev Physical Institute, Leninskii Prospect 53, 119991 Moscow, Russia
[4] Institute of Physics, University of Tartu, Riia 142, 51014 Tartu, Estonia
[5] Kurnakov Institute of General and Inorganic Chemistry, Leninskii Prospect 31,
119991 Moscow, Russia

Abstract
Vacuum ultraviolet excitation spectra at $\sim$10 K have been recorded for $4f^N \rightarrow 4f^{N-1}5d$
transitions of Cs_2NaYF_6:Ln^{3+} (Ln = Nd, Sm, Eu, Tb, Ho, Er, Tm). In these high bandgap hosts
the lanthanide ions occupy octahedral symmetry sites. The spectra comprise broad, structured
bands and in most cases the individual vibronic structure is not resolved. Simulations of the
relative intensities and band positions in the spectra have been made by using parameter values
from previous studies and/or by employing values from similar systems or estimating trends
across the lanthanide series, without data fitting or parameter adjustments. The agreement with
experimental results is reasonable except where the luminescent state being monitored is not
efficiently populated nonradiatively from the $4f^{N-1}5d$ state, or where additional bands are
present. The latter are readily assigned to charge transfer transitions or the near-excitonic band.
Comparison of the spectra has been made with those of other high symmetry lanthanide ion
systems.

(Some figures in this article are in colour only in the electronic version)

1. Introduction

Most of the tri-positive lanthanide ions, Ln^{3+}, possess
$4f^N$–$4f^{N-1}5d$ electronic transitions in the ultraviolet and
vacuum ultraviolet (VUV) spectral regions. Due to their
applications for ultraviolet lasers [1–5], scintillators [6–8],
quantum cutters [9–14] and vacuum ultraviolet [15, 16] or x-
ray [17] phosphors, their $4f^{N-1}5d$–$4f^N$ emission spectra have
recently attracted much attention. The greater availability of
synchrotron radiation has spurred renewed theoretical interest
not only in the extension of the theoretical model developed for
the $4f^N$ configuration to the $4f^{N-1}5d$ configuration [18–21],
but also in more fundamental areas such as the first-
principles analysis method [22, 23] and spin density functional
procedure [24]. Fluoride hosts possess high bandgap energies
($>$10 eV) and therefore permit the study of not only higher
$4f^N$ energy levels [25–30] but also the $4f^{N-1}5d$ energy levels
by absorption and excitation spectroscopy, although the former

technique has seldom been employed for technical reasons.
Hence there have been many previous studies of the $4f^{N-1}5d$–
$4f^N$ emission and excitation spectra of Ln^{3+} doped into
transparent fluoride hosts. Some of the early studies of
rare earth ions doped into alkaline earth fluorides have been
mentioned by Wegh *et al* [31]. Considering publications within
mainly the last decade, the most popular host has been $LiYF_4$,
which possesses S_4 site symmetry for the guest Ln^{3+} at a
single site and it has been doped with Ln = Ce [18, 32–38],
Pr [18, 33, 35, 36, 38], Nd [3, 18, 33–36, 38–43], Sm [33],
Eu [33], Gd [14, 44, 45], Tb [19, 46, 47], Dy [19, 34, 46],
Ho [19, 46], Er [8, 18, 19, 31, 34, 35, 38, 42, 44, 46–50],
Tm [8, 18, 19, 34, 35, 38, 46, 47, 51], Yb [19] and Lu [45, 51]
for VUV investigations. Some other hosts employed with
tri-positive lanthanide ions have been cubic CaF_2 doped with
Pr [33, 52–54], Nd [33], Sm [33], Gd [55, 56], Tb [47],
Er [47], Tm [47, 53] and Lu [56] and SrF_2 doped with
Nd [57], Sm, Tb, Er and Tm [58–60], but for which different

rare earth sites may be present; YF_3 doped with Pr [61]; Gd [45]; neat GdF_3 [44, 45, 62]; LaF_3 doped with Pr [61]; neat LuF_3 [45, 51, 62] and LuF_3 doped with Ce [32]; $KMgF_3$ doped with Ce [63], Pr [64]; $NaYF_4$:Nd [43]; KYF_4 doped with Pr [65], Nd [66], Er [66, 67] andTm [66, 67]; $MGdF_4$ (M = Na, K, NH_4) doped with Nd [68], Eu [69] and Tm [68]; $LiGdF_4$ [44, 45, 62] doped with Ce [44] and Eu [13]; $LiLuF_4$ [45, 62] doped with Ce [32], Pr [61, 70, 71], Nd [3, 39] and Tb [72]; K_2YF_5 doped with Pr [65]; KY_3F_{10} doped with Pr [53, 61], Nd [3] and Tm [53]; CsY_2F_7 doped with Pr [65] and Er [67]; $CsGd_2F_7$ doped with Pr [65], Tm [67] and Er [67]; LiKYF$_5$:Pr [65]; $LiKGdF_5$ doped with Er [73] and Tm [73]; $LiCaAlF_6$ doped with Ce [37, 74], Nd [75], Eu [76] and Tm [44, 77]; $LiSrAlF_6$ doped with Eu [76] and Tm [78]; BaY_2F_8 doped with Nd [3, 39] and Er [79]; BaSiF$_6$:Pr [80]; K_3YF_6:Nd [81] and CaNaYF$_6$:Ce [82]. Some of the important results from these experiments with fluoride hosts are briefly presented.

The interconfigurational spectra of Ln^{3+} are electric-dipole-allowed transitions and comprise broad bands with some superimposed sharp lines at low, and also in some cases at higher, energy. The broad structure arises not only from the superposition of pure electronic transitions but also from the presence of vibrational progressions due to the contraction in bond distance in the $4f^{N-1}5d$ configuration [83]. The real phonon spectrum of the host lattice, rather than displaced Gaussian curves [19, 36], has been employed in the simulations of low temperature absorption spectra of several systems [21, 45]. The reappearance of fine structure for high energy bands in the $4f^N$–$4f^{N-1}5d$ excitation spectra provided the realization that the $4f^{N-1}$ core and the 5d electron are not strongly coupled [47]. Such high energy structure is associated with electronic transitions where the d electron is in the lower energy level and the $4f^{N-1}$ core is highly excited. It was found that the barycenter of $4f^{N-1}5d$ absorption shifts to higher energy when the initial $4f^N$ energy level is at higher energy [40, 41]. This effect was attributed to a 'partial memory' of the initial $4f^N$ state.

The theoretical model for the $4f^N$ configuration has been extended for $4f^{N-1}5d$ to take into account atomic interactions: the direct and exchange Slater parameters for the Coulomb interaction between the 4f and 5d electrons, and the spin–orbit interaction and the crystal field interaction of the 5d electron [21, 33–36, 41]. The approximations made include the neglect of odd-parity crystal field parameters and, in the case of $LiYF_4$, the assumption of higher (D_{2d}) site symmetry of Ln^{3+}. With the inclusion of the additional interactions into the usual $4f^{N-1}$ model Hamiltonian, simulations of energies and intensities of $4f^{N-1}5d$–$4f^N$ emission and excitation spectra have been performed [18, 19, 33–36]. In these calculations, the fd Slater atomic parameters calculated from Cowan's code need to be considerably reduced due to the nephelauxetic effect. Also, the f-electron Slater and spin–orbit coupling parameters are slightly greater for the $4f^{N-1}5d$ configuration than for $4f^N$. The electric dipole matrix element for the spin-allowed transition was found to decrease considerably from Ce^{3+} to Tm^{3+} [34], due to decreased overlap between the $4f^{N-1}$ core and the delocalized 5d electron. The ions in the second half of the lanthanide series show both spin-forbidden and spin-allowed transitions, with very different lifetimes [31] and with the energy splitting between the low-spin and high-spin $4f^{N-1}5d$–$4f^N$ bands decreasing from Tb^{3+} to Tm^{3+} due to decreasing exchange interaction with increasing nuclear charge [34]. The trends in energy parameters across the lanthanide series have been reviewed [84]. On collecting the relevant $4f^N$ and 5d electron parameters for $LiYF_4$:Ln^{3+} from several publications [18, 19, 33, 35] it is interesting to observe their variation across the series. Although the magnitude of F^2(fd) (or F^4(fd)) was listed as similar for the ions Tb^{3+}, Dy^{3+}, Ho^{3+}, Er^{3+} and Tm^{3+}, the value was rather different for the three ions Nd^{3+}, Sm^{3+} and Eu^{3+}, as well as for Pr^{3+}. The same comment applies to G^1(fd), G^3(fd) and G^5(fd). In contrast, the spin–orbit coupling constant for the d electron showed a monotonic increase across the series from Ce^{3+} to Tm^{3+}. The fitted 5d crystal field parameters were found to have the same signs as the 4f parameters but were about 20 times larger because of the greater radial extension of 5d orbitals, as compared with 4f [36]. The second rank crystal field parameter B_0^2(d) and the fourth rank parameter B_0^4(d) did not show a smooth change across the lanthanide series, although overall the former decreased from Ce^{3+} to Tm^{3+} whereas the latter increased. The decreasing crystal field strength for the heavier rare earths was attributed to the lanthanide contraction [19]. Empirical rationalizations, generalizations and correlations of 5d level energies with respect to those of Ce^{3+} and the host crystal conduction band have been made by Dorenbos and co-workers and are summarized elsewhere [85].

The present study aims to further test the computational model employed for the calculations of $4f^{N-1}5d$ energy levels and $4f^N$–$4f^{N-1}5d$ transition intensities by studying the spectra of Ln^{3+} with rather different coordination geometry in cubic hexafluoroelpasolite systems. Indeed the test is rigorous because, due to the O_h site symmetry of Ln^{3+} at the unique site [86], only two $4f^N$ and one 5d crystal field parameters are employed in the calculations, compared with five and three, respectively, for the $LiYF_4$ host. Due to energy level degeneracies of up to fourfold, and restrictive O_h point group selection rules, the interconfigurational spectra were expected to be simpler than for lower symmetry hosts such as $LiYF_4$, although this was not found to be so in most cases. Furthermore, the high bandgap energy and the chemical inertness of the hexafluoroelpasolite systems make these systems attractive for the study of higher electronic configurations.

The magnetic properties [87], vibrational spectra [88] and intraconfigurational $4f^N$–$4f^N$ spectra of Nd^{3+} [89], Eu^{3+} [90, 91], Tb^{3+} [92], Er^{3+} [93], Tm^{3+} [94] and Yb^{3+} [95, 96] in lanthanide hexafluoroelpasolite systems have previously received attention. Some investigations of the $4f^{N-1}5d$–$4f^N$ spectra and/or VUV spectra of Cs_2NaLnF_6 and Cs_2NaYF_6:Ln^{3+} systems have previously been published. The results for hexafluoroelpasolite hosts doped with Ce^{3+} and Pr^{3+} are problematic because for these large cations there are several phases present in Ce^{3+}-doped Rb_2NaYF_6 [17, 97–99] and Ce^{3+} occupies several sites in the crystal of Rb_2KInF_6 [3, 99], as does Pr^{3+} in Cs_2KYF_6 [100].

The ion Tb^{3+} exhibits $4f^8$–$4f^75d$ excitation bands above $\sim37\,000\,\mathrm{cm}^{-1}$ in the Rb_2KInF_6 host (which undergoes a phase transition at low temperature so that the Tb^{3+} site symmetry is lowered to C_{2v} [3, 101]) although a spectral interpretation was not given [3, 99]. The $4f^N$–$4f^{N-1}5d$ spectra of Nd^{3+} [89], Er^{3+} [102] and Tm^{3+} [102, 103] in the Cs_2NaYF_6 host have been previously reported and are subsequently referred to with respect to the spectra obtained herein.

2. Experiment

2.1. Synthesis of the hexafluoroelpasolites

The Cs_2NaYF_6 single crystals doped with Nd^{3+} (nominal concentration 1.0 at.%—hereafter abbreviated to 1.0%), Sm^{3+} (3%), Eu^{3+} (0.3%), Gd^{3+} (6.0, 30.0 and 50.0%), Tb^{3+} (1.0%), Ho^{3+} (10.0%), Er^{3+} (10%) and Tm^{3+} (1%) were synthesized under hydrothermal conditions [90]. The crystallographic details for the cubic host lattices are available [86].

2.2. Spectral measurements

The measurements were performed at the SUPERLUMI station [104] of HASYLAB at DESY, using synchrotron radiation from the DORIS storage ring for excitation in the spectral range 70–280 nm. The excitation spectra were recorded with an instrumental resolution of ~0.3 nm. The wavelength positions of all features in excitation spectra were determined with an accuracy better than 0.05 nm. A 0.3 m Czerny–Turner monochromator-spectrograph SpectraPro-308i (Acton Research Inc.) with an R6358P (Hamamatsu) photomultiplier tube was applied for selecting the monitored wavelength when measuring excitation spectra.

The crystals were cleaved prior to mounting onto the sample holder in a flow-type liquid helium cryostat. The crystallographic axes of the crystals when installed onto the sample holder were not oriented with respect to the polarization vector of exciting radiation. All measurements have been performed under ultra-high-vacuum conditions.

3. Theoretical

The standard phenomenological crystal field Hamiltonian and its extension given in [33] were used to calculate the $4f^N$ and $4f^{N-1}5d$ multi-electron energy levels. The parameter values (using the standard notations given in [33]) to describe the various interactions are listed in table 1.

Some remarks concerning the choice of parameter values for LnF_6^{3-} are pertinent because the spectra were not subjected to an optimized fitting, but were simulated by a reasonable choice of parameter values. First the $4f^N$ parameters are mentioned. The parameters for the $4f^8$ configuration of Tb^{3+} were obtained from a new fitting of the energy levels reported for Cs_2NaTbF_6 by Berry *et al* [92]. The parameters for Er^{3+} [93] and Tm^{3+} [94] are available. The parameters given for Cs_2NaYF_6:Nd^{3+} [89] were used. There are no parameter values available for Sm^{3+}, Gd^{3+} and Ho^{3+} so that the values from $LnCl_6^{3-}$ were used for the host-insensitive free ion
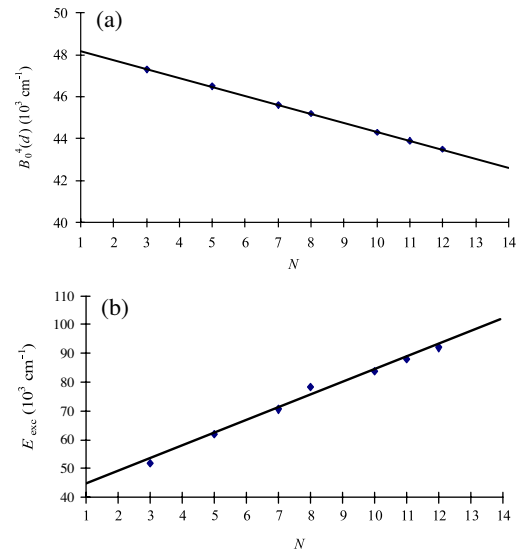
Figure 1. Plots of E_{exc} and $B_0^4(\mathrm{d})$ against N, number of $4f^N$ electrons in Ln^{3+} for Cs_2NaYF_6:Ln^{3+}. The plot for (a) is $B_0^4(\mathrm{d}) = -426.56N + 48\,598$. The fit for (b) is $E_{\mathrm{exc}} = 39\,121 + 4568N$; $R^2 = 0.992$.

parameters whereas for the crystal field parameters the values for Sm^{3+} were estimated from those for $SmCl_6^{3-}$ using the ratios for $EuCl_6^{3-}$ [105], i.e., $B_0^4(SmF_6^{3-}) = 1.5B_0^4(SmCl_6^{3-})$ and $B_0^6(SmF_6^{3-}) = 1.7B_0^6(SmCl_6^{3-})$; the values for Gd^{3+} were estimated from those for $GdCl_6^{3-}$ [105] using the average ratios for Eu^{3+} and Tb^{3+}, i.e. $B_0^4(GdF_6^{3-}) = 1.77B_0^4(GdCl_6^{3-})$ and $B_0^6(GdF_6^{3-}) = 1.42B_0^6(GdCl_6^{3-})$; the values for Ho^{3+} were estimated from those for $HoCl_6^{3-}$ [105] using the ratios for Er^{3+}, i.e. $B_0^4(HoF_6^{3-}) = 1.73B_0^4(HoCl_6^{3-})$ and $B_0^6(HoF_6^{3-}) = 1.42B_0^6(HoCl_6^{3-})$. It is noted that the $4f^N \rightarrow 4f^{N-1}5d$ absorption spectra are not very sensitive to the values of those parameters.

Concerning the parameters for the $4f^{N-1}5d$ configuration of LnF_6^{3-}, $B_0^4(\mathrm{d})$, the cubic crystal field parameter for the 5d electron, was estimated by scaling the $B_0^4(\mathrm{d})$ parameter for $CeCl_6^{3-}$ [105] by the factor of 1.25 [106] and then decreasing it appropriately across the series using the same ratio as for CaF_2 [19]. The ensuing linear relationship of $B_0^4(\mathrm{d})$ with the number N in $4f^N$ is shown in figure 1(a). This is the most important parameter for the structure of the f–d absorption spectra concerning the $5d(t_{2g})$–$5d(e_g)$ splitting. The absorption spectra thus obtained are suitable for the indication of the absorption to 5d e_g orbitals, which are usually not so well resolved in the excitation spectra.

The F^2, F^4, F^6 and ζ_{4f} parameters for the $4f^{N-1}$ core were scaled from the corresponding parameters for the $4f^N$ configuration by the factor 1.06 to account for the contraction of 4f orbitals. The other core parameters, i.e. T^i, M^0, P^2, B_0^4 and B_0^6, are less important and were assigned the same values as those for $4f^N$. It is noted that there are no T^i parameters for the $4f^2$ core of Nd^{3+} and the T^i parameters for the $4f^{11}$ core of Tm^{3+} were assigned the values for the $4f^{11}$ configuration of Er^{3+}.

Turning to the parameters for the 5d electron, the calculated Hartree–Fock (HF) values were used for ζ_{5d},

Table 1. Energy parameters (in cm^{-1}) used for the calculation of 4f^N–4f^{N-1}5d absorption line strengths. Refer to section 3 for explanation.

	Parameter	Nd^{3+}	Sm^{3+}	Eu^{3+}	Gd^{3+}	Tb^{3+}	Ho^{3+}	Er^{3+}	Tm^{3+}
4f^N	F^2	72 188	78 165	83 897	78 686	86 758	94 584	97 398	101 576
	F^4	52 625	56 612	59 986	70 120	62 610	67 847	68 093	71 602
	F^6	35 372	40 172	41 361	43 596	49 470	47 274	55 532	50 563
	ζ_{4f}	871	1 166	1 327	1 505	1 694	2 130	2 327	2 639
	α	21	22	16.8	37	23	15	18	17
	β	−593	−717	−640	−1 905	−1 029	−599	−570	−625
	γ	1 445	1 564	1 750	1 679	1 608	1 884	1 631	1 820
	M^0	2.11	2.13	2.4	1.59	2.84	3.00	3.60	1.15
	P^2	192	2 600	245	—	498	523	653	0
	T^2	298	256	370	—	523	287	451	451
	T^3	35	26	40	—	2	37	61	61
	T^4	59	22	40	—	38	98	100	100
	T^6	−285	−141	−330	—	−235	−313	−245	−245
	T^7	332	246	380	—	367	421	305	305
	T^8	305	382	370	—	450	351	160	160
	B_0^4	3 742	1 671	2 993	3 144	3 323	2 756	2 696	2 571
	B_0^6	452	207	428	197	230	327	294	265
4f^{N-1}5d	E_{exc}	52 000	62 000	68 000	70 560	78 300	83 800	88 000	92 000
	B_0^4 (d)	47 300	46 500	46 000	45 600	45 200	44 300	43 900	43 500
	η_{fd}	0.55	0.55	0.55	0.55	0.55	0.55	0.55	0.55
	ζ_{5d}	1 216	1 351	1 419	1 488	1 557	1 697	1 768	1 839

following van Pieterson *et al* [19]. Values for the parameters describing the Coulomb interaction between the 4f^{N-1} core and the 5d electron, F^k(fd) ($k = 2, 4$) and G^k(fd) ($k = 1, 3, 5$) were scaled from the HF values by the factor of $\eta_{fd} = 0.55$, optimized for the splitting between high-spin and low-spin states in TbF$_6^{3-}$. The parameter E_{exc}, which describes the position of the barycenter of 4f^{N-1}5d relative to that of 4f^N, was fine-tuned to give the measured onset of 4f^N–4f^{N-1}5d absorption. The linear relationship of E_{exc} with N in 4f^N is depicted in figure 1(b).

The transitions between 4f^N and 4f^{N-1}5d are electric-dipole-allowed and it is straightforward to calculate the matrix elements of the electric dipole moment operator between multi-electron wavefunctions of 4f^N and 4f^{N-1}5d. There is generally a displacement for the equilibrium positions of ligands in 4f^N–4f^{N-1}5d transitions which results in the vibrational progression structure of the absorption and emission spectra, which is unresolved as broad bands with Stokes shifts. Since the detailed vibronic structures are not resolved, we adopted their crude simulation proposed by van Pieterson *et al* [33], i.e. by using Gaussian curves, displaced towards higher energy from the zero-phonon lines by $E_{shift} = 600$ cm^{-1} and $E_{width} = 1000$ cm^{-1}, as estimated from the experimental spectra.

4. Results and discussion

The ∼10 K excitation spectra of Sm^{3+}, Eu^{3+}, Gd^{3+}, Tb^{3+} and Ho^{3+} diluted into Cs$_2$NaYF$_6$ are presented in this section, together with simulated spectra for Nd^{3+}, Er^{3+} and Tm^{3+} for which experimental results have previously been published. The boundary energy separating Ln^{3+}4f^N–4f^{N-1}5d transitions and Cs$_2$NaYF$_6$ host absorption is located at ∼88 500 cm^{-1}. Characteristic bands are observed in all of the spectra, including a broad band at 120 nm, which corresponds to the near-excitonic band (direct optical creation of excitons),

and other features of host excitation at higher energies. A brief discussion of charge transfer (CT) transitions is given in section 4.1 and this is followed by discussions of the excitation spectra in sections 4.2–4.9.

4.1. Charge transfer (CT) transitions

Besides 4f^N–4f^{N-1}5d absorption transitions in the VUV region, transitions due to F^-–Ln^{3+} CT are also expected. The measured and estimated lowest 4f^N–4f^{N-1}5d absorption energy, E_{4f-5d}, and charge transfer energy, E_{CT}, for lanthanide ions in Cs$_2$NaYF$_6$:Ln^{3+} are listed in table 2. Since the onset of 4f → 5d absorption of Ce^{3+} in Cs$_2$NaYF$_6$:Ce^{3+} is not available, the equation:

$$E_{4f-5d}(Ln^{3+}) = E_{4f-5d}(Tb^{3+}) + \Delta E_{4f-5d}(Ln^{3+}, Ce^{3+}) - \Delta E_{4f-5d}(Tb^{3+}, Ce^{3+}) \tag{1}$$

was used to calculate the lowest 4f^N–4f^{N-1}5d absorption energy for all ions using the experimental Tb^{3+} E_{4f-5d} value from herein and the values ΔE_{4f-5d} given by Dorenbos [107]. For Tb^{3+}, the onset of 4f^8 → 4f^{7}5d absorption is given in table 2 under the column E_{4f-5d} (expt) and also in square brackets under the column E_{4f-5d} (calc). The equation:

$$E_{CT}(Ln^{3+}) = E_{CT}(Eu^{3+}) + \Delta E_{CT}(Ln^{3+}, Eu^{3+}) \tag{2}$$

was used to calculate the maximum of the F$^-$–Ln^{3+} CT band for all ions using the Eu^{3+} E_{CT} (expt) value and ΔE_{CT} given by Dorenbos [108]. The calculated E_{CT}(Eu^{3+}) value is actually the measured value for Cs$_2$NaYF$_6$:Eu^{3+} herein and is given in table 2 in square brackets. The value is fairly close to that reported for LiCaAlF$_6$:Eu^{3+} [76]. The E_{CT} (expt) value for Tm^{3+} is the value for this ion in the host LiCaAlF$_6$ [108] (given in [77]) and is expected to be a reasonable approximation (with errors up to a few thousand of cm^{-1}) judging from the small variation of F$^-$–Eu^{3+} CT band energies in various hosts [109].

Table 2. The measured and estimated (using phenomenological models) lowest $4f^N$–$4f^{N-1}5d$ absorption energy E_{4f-5d} and charge transfer (CT) energy E_{CT} for lanthanide ions in Cs_2NaYF_6:Ln^{3+}. (Refer to equations (1) and (2) for the definitions of symbols).

Ln^{3+}	ΔE_{4f-5d} 10^3 cm^{-1}	E_{4f-5d} (calc) 10^3 cm^{-1}	nm	E_{4f-5d} (expt) 10^3 cm^{-1}	nm	ΔE_{CT} 10^3 cm^{-1}	E_{CT} (calc) 10^3 cm^{-1}	nm	E_{CT} (expt) 10^3 cm^{-1}	nm
Ce^{3+}	[0]	32.1	312							
Pr^{3+}	12.2	44.3	226			19.7	79.9	125		
Nd^{3+}	22.7	54.8	182	52.6	190	18.5	78.7	127	82.6	121
Sm^{3+}	26.5	58.6	171	56.8	176	9.4	69.6	144		
Eu^{3+}	35.9	68.0	147			[0]	[60.2]	[166]	60.2	166
Gd^{3+}	45.8	77.9	128	75.8	132					
Tb^{3+}	13.2	[45.3]	[221]	45.3	221					
	(5.5)	(37.6)	(266)	(37.4)	(267)					
Dy^{3+}	25.1	57.2	175			16.4	76.6	131		
	(17.7)	(49.8)	(201)							
Ho^{3+}	31.8	63.9	156	62.1	161	19.5	79.7	125		
	(29.1)	(61.2)	(163)	(58.5)	(171)					
Er^{3+}	30.0	62.1	161			18.2	78.4	128		
	(27.0)	(59.1)	(169)	(58.8)	(170)					
Tm^{3+}	29.0	61.1	164	60.6	165	13.5	73.7	136	~80.6	~124
	(27.0)	(59.1)	(169)	(58.4)	(171)					
Yb^{3+}	38.0	70.1	143			3.5	63.7	157		

The data in round parentheses in table 2 for the ions from Tb^{3+} to Yb^{3+} represent the energies of the onset of spin-forbidden $4f^N$–$4f^{N-1}5d$ absorption.

4.2. Spectra of Cs_2NaYF_6:Nd^{3+}

The 9 K VUV excitation spectra of Nd^{3+} in several hexafluoroelpasolite lattices have been previously reported [89]. The experimental spectrum (full line, figure 2(a)) comprises two groups of bands with their peaks separated by ∼27 000 cm^{-1}. Saturation occurs for the lower energy group between 172 and 192 nm. The simulation shown in figure 2(a) (dashed line) utilizes similar parameters to those in [89] except that the 5d crystal field parameter has been increased by the factor 1.23. The poorer fit for the bands between 116 and 140 nm is attributed to the less efficient energy transfer to the emitting $4f^3{}^2G(2)_{9/2}$ multiplet term when the initial $4f^25d$ level is at a much higher energy.

4.3. Spectra of Cs_2NaYF_6:Sm^{3+}

The excitation spectrum for Cs_2NaYF_6:Sm^{3+} (3%) at 12.4 K when monitoring the emission from the $4f^5$ state ($^4G_{5/2}$ + $^4F_{5/2}$), λ_{em} = 598.6 nm, is shown in figure 2(b). The initial 'zero-phonon line' is at 174.9 nm (57 175 cm^{-1}). The term 'zero-phonon line' (subsequently 'ZPL') refers to the fact that vibrational structure is not resolved so that its location by taking the convoluted band maximum may not correspond to the real zero-phonon line (i.e. 0–0 transition). On closer inspection, the step-like appearance of a vibrational progression between 175 and 170 nm does not give progressive vibrational frequencies as expected for the totally symmetric Sm–F stretching vibration, ν_s (Sm–F), so that other electronic transitions are present. Then to higher energy, further transitions produce unresolved structures between 162 and 170 nm. A vibrational progression is observed at the high energy side of this structure, starting with the ZPL at 161.5 nm

(presumably corresponding to the simulated band D) with the initial vibrational quantum of 470±10 cm^{-1}, which apparently decreases with successive members. The vibrational frequency is similar to the value expected from the ground state (Raman spectrum [88]) but the measurement performed herein with moderate resolution does not permit an exact comparison. A new transition is clearly observed at 156.0 nm (presumably corresponding to E) with the initial progression frequency ∼460 cm^{-1}. Two other groups of bands are at higher energy. The first group is partially resolved between 134 and 145 nm, whereas the second group is stronger and broader between 116 and 134 nm. The final states marked in figure 2(b) belong to A$_1$–E: $^6[(^5I)t_{2g}]$; F–G: $^6[(^5F)t_{2g}]$; I–J: $^6[(^5G)t_{2g}]$ and K: $^6[(^5K)e_g]$.

4.4. Spectra of Cs_2NaYF_6:Eu^{3+}

Figure 2(c) compares the excitation spectra of the $^5D_0 \rightarrow {}^7F_1$ emission of Eu^{3+} in Cs_2NaYF_6:Eu^{3+} (0.3%) at 7.8 and 300 K. The simulated $4f^6 \rightarrow 4f^55d^1$ transitions are shown underneath and show the absence of two broad bands above. Unlike the interconfigurational transitions, which do not exhibit marked wavelength shifts with decreasing temperature, these two broad bands are distinguished by their shifts to shorter wavelengths: from 167 to 162 nm, and from 125 to 122 nm. Of the two bands, the longer wavelength one corresponds to the Eu^{3+}–F^- CT transition whilst the shorter wavelength one is the near-excitonic transition.

The final states marked in the simulation of figure 2(c) correspond to A, B: $^7[^6H, t_{2g}]$; C: $^7[^6F, t_{2g}]$ and D, E: $^7[^6H, e_g]$. The transitions to the latter states, D, E, lie above the bandgap so that they are not observed. The simulation predicts four major bands in the spectrum but it does not agree well with the fine structure in the low temperature spectrum partly because of our simplified treatment of phonon sidebands. Furthermore, the 7.8 K spectrum does not resolve individual vibronic progression structure with a distinct interval, but
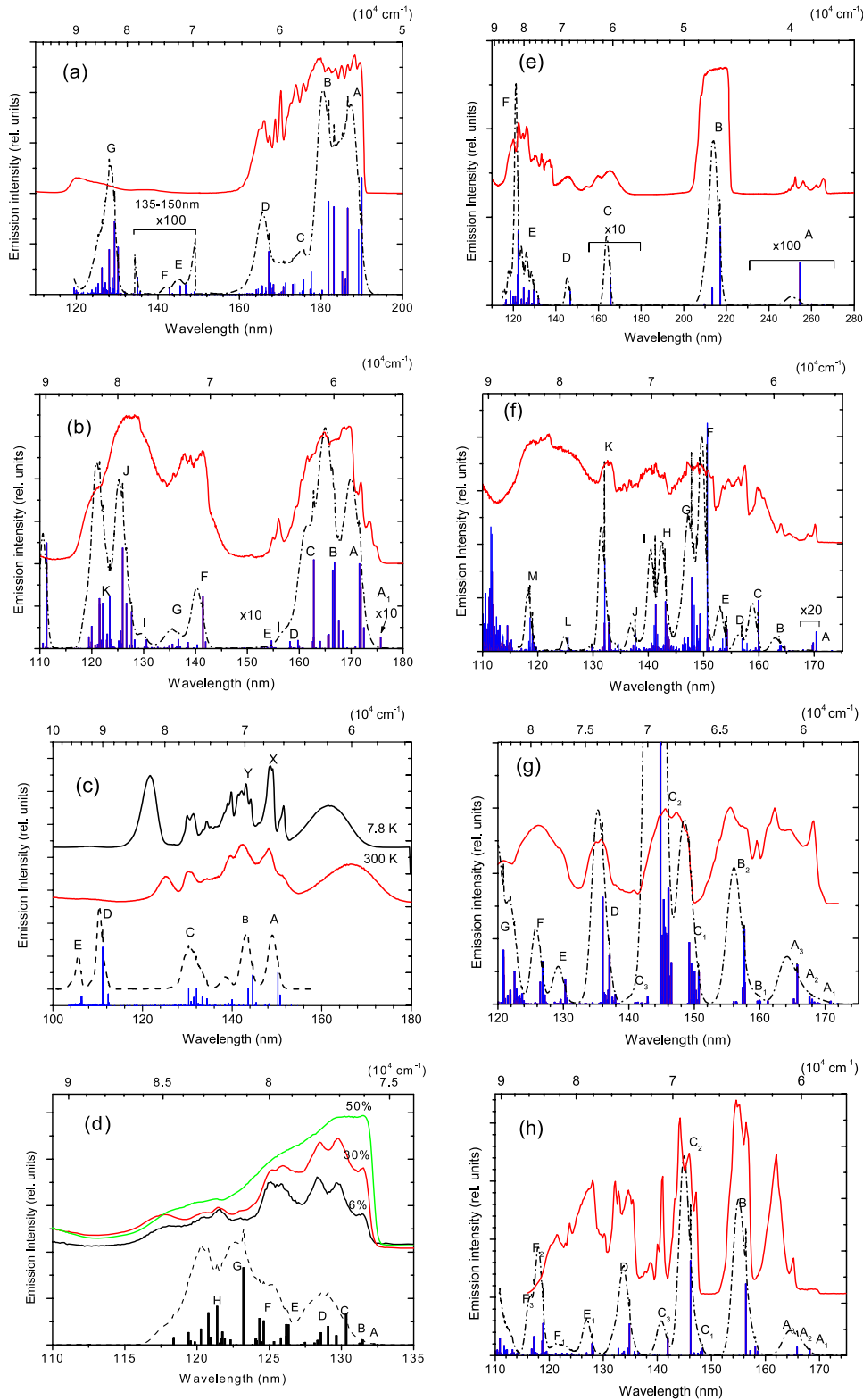
Figure 2. Experimental excitation spectra (full lines) and simulated $4f^N$–$4f^{N-1}5d$ absorption spectra (dashed lines) for $Cs_2NaYF_6:Ln^{3+}$. The vertical bars show the calculated locations and relative intensities of pure electronic transitions. The simulated convolutions follow [19] and employ $E_{shift} = 600$ cm^{-1} and $E_{width} = 1000$ cm^{-1}. Refer to the text for the explanations of labels. (a) Ln = Nd, $\lambda_{em} = 289$ nm, $T = 9$ K. Notice the ordinate scale expansion in the simulated spectrum between 135 and 150 nm; (b) Ln = Sm, $\lambda_{em} = 598.6$ nm, $T = 12.4$ K. The zero-phonon lines are enlarged by 10 times for clearer display in the ranges 175–180 nm and 145–156 nm; (c) Ln = Eu, $\lambda_{em} = 591$ nm, $T = 7.8$ and 300 K. (d) Ln = Gd, $\lambda_{em} = 313$ nm, $T = 8.9$ K (6%), $T = 8.2$ K (30%), $T = 8.2$ K (50%). The ordinate scales are arbitrary for the three concentrations. (e) Ln = Tb, $\lambda_{em} = 541$ nm, $T = 12.6$ K. The simulated intensities in the regions between 155 and 180 nm and 230 and 270 nm are enlarged by factors of 10 and 100, respectively. (f) Ln = Ho, $\lambda_{em} = 559$ nm, $T = 12.3$ K. In the region between 167 and 175 nm the intensities are enlarged by 20 times in the simulation. (g) Ln = Er, $\lambda_{em} = 175$ nm, $T = 10$ K. (h) Ln = Tm, $\lambda_{em} = 177$ nm, $T = 10.5$ K.

shows convoluted bands of different electronic transitions. The simulated transitions to A and B each comprise two intense zero-phonon lines, which are separated by 221 cm^{-1} (for A) and 482 cm^{-1} (for B). The observed splittings of the bands marked X and Y are 243 cm^{-1} and 504 cm^{-1}, respectively, which could correspond to the separations of the convoluted structure of A and B.

4.5. Spectra of Cs$_2$NaYF$_6$:Gd^{3+}

Figure 2(d) shows the excitation spectrum of Cs$_2$NaYF$_6$:Gd^{3+} between 8.2 and 8.9 K for three different dopant ion concentrations whilst monitoring the $4f^7$ $^6P_{7/2}$ $\rightarrow$ $^8S_{7/2}$ emission at 313 nm. The features are more clearly resolved for the 6% doping and consist of structured bands between 114 and 132 nm. Calculations show that there are many bands in this region and these are labeled as A–H in figure 2(d). All these bands are due to the splitting of the high-spin $^8[(^7F)t_{2g}]$ states mainly under 4f and 5d spin–orbit interactions. The simulated absorption spectrum shows poor agreement with the experimental excitation spectrum. This is attributed to the closeness of the $4f^7$ $\rightarrow$ $4f^65d$ transitions to the host bandgap where photoionization occurs and where other competing processes, such as excitonic and defect absorption, can compete with 4f–5d absorption. In fact, the transition intensities become more under-estimated on progressing from the lowest energy transition up to higher energy. The simulation predicts a second group of bands between 93 and 105 nm with comparable integrated intensity to that of the first group but these features lie above the edge of the host absorption, preventing their experimental observation under one-photon excitation.

4.6. Spectra of Cs$_2$NaYF$_6$:Tb^{3+}

The lanthanide ions of the second half of the series possess the possibilities of both spin-forbidden and spin-allowed 4f–5d transitions (or transitions to both high-spin and low-spin 5d states). For Tb^{3+}, the $4f^7$ ^8S core can couple with the 5d t_{2g} electron to give ^9D and ^7D multiplets, and by Hund's rule the former is lower in energy. Since the electronic ground state of the $4f^8$ configuration is $^7F_6$, the lower energy transitions to ^9D are expected to be much weaker than the higher energy ones to ^7D. Figure 2(e) (upward shifted solid curve) shows the 12.6 K excitation spectrum of Cs$_2$NaYF$_6$:Tb^{3+}(1%) by monitoring the $^5D_4$ $\rightarrow$ $^7F_5$ emission at 541 nm. The mainly spin-forbidden group of bands is observed as a structured group between 245 and 267 nm. Only three electronic transitions are expected in this region [110] and these can be assigned to the three groups of bands. Three features were observed in the same region in the 7 K absorption spectrum of Rb$_2$KInF$_6$:Tb^{3+} (1%) but in that case the Tb^{3+} ion is situated at a distorted octahedral site [101]. In figure 2(e), the highest energy group of spin-forbidden bands (246.5–252.6 nm) is the most clearly resolved and the initial ν_s (Tb–F) vibrational quantum based upon the ZPL is ~475 cm^{-1}, compared with the ground state value of 468 cm^{-1} [92]. Additional structure is observed with the derived vibrational energy of 225 cm^{-1}. The assignment of structure in the $4f^8$–$4f^75d$ absorption spectrum

of Cs$_2$NaTbCl$_6$ was to breathing modes of the second and third coordination shells of Tb^{3+}. It is not clear whether the band at 225 cm^{-1} in the present case corresponds to the maximum of unresolved bands, or to a single feature. The frequency is higher than the ground state t_{2g} moiety mode in Cs$_2$NaTbF$_6$ (194 cm^{-1} [92]). The lowest energy group of spin-forbidden bands (between 260 and 268 nm) is broader with a separation of ~472 cm^{-1}. A major difference with the corresponding spectra of Cs$_2$NaTbCl$_6$ is that the maximum intensity of the totally symmetric mode vibrational progression upon the electronic origin is at the $v = 0$ member in the present case, compared with $v = 1$ for the chloride. This indicates a smaller change in the configuration coordinate diagram between the ground and excited state equilibrium nuclear configurations in the present case.

The total intensity saturation of the bands between 224 and 201 nm is indicative of transitions to the terminal low-spin states. There is then a spectral window until the next group of bands at higher energy commences at 174 nm.

The calculated f–d absorption line strengths are shown below the experimental spectrum, figure 2(e), with sticks being zero-phonon lines and the dashed–dotted curve being the convolution as described above. The calculation is enlarged for better display in the ranges from 155 to 180 nm and 230 to 270 nm by 10 and 100 times, respectively. The final states belong to A: $^9[(^8S)t_{2g}]$, B: $^7[(^8S)t_{2g}]$, C: $^9[(^8S)e_g]$, D: $^7[(^8S)e_g]$, E: $^7[(^6P)e_g]$ and F: $^7[(^6I)e_g]$. The calculations show that A contains three groups, with the second and third groups being calculated to be weaker and, at 830 cm^{-1} and 1650 cm^{-1}, lower in energy than the first group, respectively.

4.7. Spectra of Cs$_2$NaYF$_6$:Ho^{3+}

Figure 2(f) shows the 12.3 K excitation spectrum of Cs$_2$NaYF$_6$:Ho^{3+} (10%) by monitoring the $^5S_2$ $\rightarrow$ $^5I_8$ emission at 559 nm. The onset of absorption is at 170.6 nm and the first band (at 170.2 nm; 58 760 cm^{-1}) has a repeating interval of 455 cm^{-1}. A broad feature is observed between these two bands, at ~290 cm^{-1} above the lowest energy band. Clearly, these weak features correspond to spin-forbidden transitions. The remaining spectrum, between 113 and 167 nm, comprises several groups of bands with some structure and consists of many overlapping transitions. The lower sticks and dashed–dotted convolution show the theoretical simulation of this structure and the calculation is enlarged for better display in the range 167–175 nm by 20 times. The calculated $4f^95d$ levels start at 57 600 cm^{-1}. The regions A–D are dominated by transitions to high-spin $^7[(^6H)t_{2g}]$ terminal states, whereas E–G correspond to low-spin $^5[(^6H)t_{2g}]$ terminal states. Region H corresponds to $^5[(^6F)t_{2g}]$, whereas I ($^7[(^6H)e_g]$) may not be efficient for excitation due to delocalization of the e_g orbitals. Region J is a mixture of $^5[(^4F(3))t_{2g}]$ and $^7[(^6H)e_g]$. Region M presumably corresponds to the 'hump' at 121.9 nm on the observed broad band between 130 and 113 nm. This broad band, with a maximum at 119 nm, is assigned to the excitonic transition, but it is at a similar energy to the F$^-$–Ho^{3+} CT transition, which is estimated from section 4.1 to center at ~118 nm.

4.8. Spectra of Cs₂NaYF₆:Er³⁺

The 10 K excitation spectrum of Cs_2NaYF_6:Er^{3+} (10%) when monitoring 5d–4f emission at 175 nm [102] is shown in figure 2(g) and it is more clearly resolved and consists of structured bands between 120 and 170 nm. The calculated $4f^{10}5d$ levels start at 58 400 cm⁻¹ (171 nm). The regions marked in figure 2(g) have the following terminal state correspondences: A_1–A_3: dominated by $^6[(^5I)t_{2g}]$; B_1, B_2 and C_3: $^6[(^5I)t_{2g}]$ with a considerable mixture of $^4[(^5I)t_{2g}]$; C_1, C_2, D: $^4[(^5I)t_{2g}]$; E and F: $^5[(^5F)t_{2g}]$; where the 5d electron is in the lower t_{2g} orbital throughout. By contrast, the terminal state of G is $^6[(^5I)e_g]$, which may not be efficient due to delocalization of the e_g orbital. The CT band is predicted to be near 120 nm.

4.9. Spectra of Cs₂NaYF₆:Tm³⁺

The spectrum of Cs_2NaYF_6:Tm^{3+} has previously been simulated [103] and is included herein for completeness, using different parameter values. The 10.5 K excitation spectrum of Cs_2NaYF_6:Tm^{3+} (1%) by monitoring the $4f^{11}5d \rightarrow 4f^{12}$ emission is shown in the upper part of figure 2(h), together with the simulation underneath. The $4f^{12}$ ground multiplet term of Tm^{3+} is $^3H_6$. The calculated $4f^{11}5d$ levels start at 58 300 cm⁻¹ (171.5 nm), with mainly high-spin states A_1–A_3, C_1 and C_3, which are dominated by $^5[(^4I)t_{2g}]$. Regions B, C_2 and D are dominated by low-spin final states $^3[(^4I)t_{2g}]$. To higher energy, the bands E_1 (terminal state $^3[(^4F)t_{2g}]$), F_1 and F_3 ($^3[(^2H(2))t_{2g}]$) all represent excited $4f^{11}$ core states with the d electron in the lower t_{2g} orbital. The simulation shows good agreement between 130 and 160 nm but the expected strong excitation transition (F_2) to the $^3[(^4I)e_g]$ terminal state may not be efficient due to delocalization of the e_g orbitals. The feature in the region 115–135 nm is assigned to the CT band, which is estimated to peak around 124 nm. The differences with the previous simulation in [103] are mainly to short wavelengths of 138 nm. The parameters employed are rather different from those in [103], particularly for the 5d crystal field parameter, which is reduced by 13%.

5. Conclusions

The ∼10 K VUV excitation spectra of tri-positive lanthanide ions in the LnF_6^{3-} moiety situated at octahedral sites of the hexafluoroelpasolite host have been presented and analyzed herein. The host lattices employed are particularly suitable for probing the $4f^{N-1}5d$ configurations due to their chemical inertness and high energy bandgap. Most of the observed structure represents electric-dipole-allowed $4f^N \rightarrow 4f^{N-1}5d$ transitions, together with vibrational structure based upon them. In nearly all cases, the ensuing spectral congestion from many overlapping transitions does not permit a detailed analysis to be made of individual electronic transitions. The theoretical calculations have provided reasonable interpretations of the experimental results, with some additional bands not present in the simulations corresponding to CT and excitonic transitions. The calculations were not performed by data fitting but rather

by selection of parameters from previous studies or by extrapolation of a trend throughout the lanthanide series.

It is instructive to compare the present results with those from other fluoride systems doped with lanthanide ions. However, nearly all of the systems mentioned in section 1 correspond to low symmetry environments of Ln^{3+} and the comparison is not meaningful. There are two exceptions. First, the VUV excitation spectra of Tm^{3+} in the $LiMAlF_6$ (M = Ca, Sr) hosts [77, 78], and the VUV absorption spectrum of Nd^{3+} in $LiCaAlF_6$ [75], have been reported. In this host, the Ln^{3+} ions are situated at the Ca^{2+} D_{3d} site in a trigonally elongated octahedral coordination. There is a clear one-to-one correspondence of the first four groups of $4f^{12} \rightarrow 4f^{11}5d$ bands for Tm^{3+} in these hosts and in the Cs_2NaYF_6 host. However, as also for the $4f^3 \rightarrow 4f^25d$ spectrum of Nd^{3+}, all of the bands are situated at higher energies in the $LiCaAlF_6$ host than in the elpasolite. True *et al* [77] have remarked that the peak energy of the first fd band depends on the crystal field splitting, increasing with increasing Ln–F bond distance. In fact, the Ca–F distance (229 pm) [111] in the $LiCaAlF_6$ host is a little longer than the Y–F distance (227 pm) in Cs_2NaYF_6. It is interesting that, by adjusting the Ln–F distance in similar host lattices, the absorption band positions could therefore be tuned.

The second comparison is made with the CaF_2 host, where at low dopant ion concentrations (∼0.001 at.%), Ln^{3+} is situated at the center of a cube of F^- ions [33], although other sites and clusters dominate at higher concentrations [54–56]. The eight-coordination O_h symmetry environment again provides the splitting of the d-electron orbitals into e_g and t_{2g} representations, but the ordering of these two is the opposite of the present study. Without considering fine structure, the features in the lower region of the VUV excitation spectra of MF_2 (M = Ca, Sr) doped with Nd^{3+} and Sm^{3+} [33, 58] are generally similar, and at similar wavelengths, to the present spectra. This is because the structure corresponds to the coupling of the $4f^{N-1}$ core with a given 5d orbital for the lowest crystal field level and is mainly due to the interactions in the $4f^{N-1}$ core and the exchange interaction between $4f^{N-1}$ and the given 5d orbital [112–114] which do not change appreciably for the fluoride hosts. In the case of Tb^{3+}, the first spin-allowed and spin-forbidden transitions are at similar wavelengths in the Cs_2NaYF_6 and MF_2 [18, 58, 59] hosts. The detailed structure of the spin-forbidden transition is different, however. For CaF_2:Tb^{3+} [18] there are two groups of bands whereas there are three groups in figure 2(e). The difference lies in the selection rules for the O_h molecular point group since only transitions to terminal states with T_{1u} irreps are electric-dipole-allowed. Coupling the ^8S core with t_{2g} or e_g orbitals gives three or two T_{1u} states, respectively.

As in the present study, the parameter values for modeling the spectra of CaF_2:Ln^{3+} were not fitted. The 5d crystal field parameter was taken from the fit to the corresponding spectra of Ce^{3+} and then scaled across the lanthanide series. Its magnitude is slightly greater in the present simulations. Compared with the $4f^N$ parameters for CaF_2:Ln^{3+}, the magnitude of the fourth-order crystal field parameter is greater herein (with opposite sign), whereas the (smaller) sixth-order parameter is smaller for the elpasolites.

Acknowledgments

References

[1] Nicolas S, Descroix E, Joubert M F, Guyot Y, Laroche M, Moncorge R, Abdulsabirov R Y, Naumov A K, Semashko V V, Tkachuk A M and Malinowski M 2003 *Opt. Mater.* **22** 139
[2] Dubinskii M A, Semashko V V, Naumov A K, Abdulsabirov R Yu and Korableva S L 1993 *J. Mod. Opt.* **40** 1
[3] Joubert M F, Guyot Y, Jacquier B, Chaminade J P and Garcia A 2001 *J. Fluor. Chem.* **107** 235
[4] Mroczkowski S and Dorain P 1985 *J. Less-Common Met.* **110** 259
[5] Dubinskii M A, Semashko V V, Naumov A K, Abdulsabirov R Yu and Korableva S L 1993 *Laser Phys.* **3** 216
[6] Blasse G 1991 *IEEE Trans. Nucl. Sci.* **38** 30
[7] Nikl M 2006 *Meas. Sci. Technol.* **17** R37
[8] Becker J, Gesland J Y, Kirikova N Yu, Krupa J C, Makhov V N, Runne M, Queffelec M, Uvarova T V and Zimmerer G 1998 *J. Alloys Compounds* **275–277** 205
[9] Oskam K D, Wegh R T, Donker H, Van Loef E V D and Meijerink A 2000 *J. Alloys Compounds* **300** 421
[10] Meijerink A, Wegh R, Vergeer P and Vlugt T 2006 *Opt. Mater.* **28** 575
[11] Peijzel P S and Meijerink A 2005 *Chem. Phys. Lett.* **401** 241
[12] Lee T-J, Luo L-Y, Cheng B-M, Diau W-G and Chen T-M 2008 *Appl. Phys. Lett.* **92** 081106
[13] Wegh R T, Donker H, Oskam K D and Meijerink A 1999 *Science* **283** 663
[14] Wegh R T, Donker H, Meijerink A, Lamminmäki R and Hölsä J 1997 *Phys. Rev.* B **56** 13841
[15] Toda K 2006 *J. Alloys Compounds* **408–412** 665
[16] Jüstel T, Krupa J-C and Wiechert D U 2001 *J. Lumin.* **93** 179
[17] Pawlik Th and Spaeth J-M 1997 *J. Appl. Phys.* **82** 4236
[18] Piejzel P S, Vergeer P, Meijerink A, Reid M F, Boatner L A and Burdick G W 2005 *Phys. Rev.* B **71** 045116
[19] van Pieterson L, Reid M F, Burdick G W and Meijerink A 2002 *Phys. Rev.* B **65** 045114
[20] Gâcon J C 2003 *Opt. Mater.* **24** 209
[21] Malkin B Z, Solovyev O V, Malishev A Yu and Saikin S K 2007 *J. Lumin.* **125** 175
[22] Ishii T, Fujimura K, Sato K, Brik M G and Ogasawara K 2004 *J. Alloys Compounds* **374** 18
[23] Ishii T, Brik M G and Ogasawara K 2004 *J. Alloys Compounds* **380** 136
[24] Stephan M, Zachau M, Gröting M, Karplak O, Eyert V, Mishra K C and Schmidt P C 2006 *J. Lumin.* **114** 255
[25] Wegh R T, Van Loef E V D, Burdick G W and Meijerink A 2003 *Mol. Phys.* **101** 1047
[26] Vergeer P, Babin V and Meijerink A 2005 *J. Lumin.* **114** 267
[27] Srivastava A M and Duclos S J 1997 *Chem. Phys. Lett.* **275** 453
[28] Ellens A, Kroes S J, Sytsma J, Blasse G and Khaidukov N M 1991 *Mater. Chem. Phys.* **30** 127
[29] Peijzel P S, Vermeulen P, Schrama W J M, Meijerink A, Reid M F and Burdick G W 2005 *Phys. Rev.* B **71** 125126
[30] Wegh R T, Meijerink A, Lamminmäki R-J and Hölsä J 2000 *J. Lumin.* **87–89** 1002
[31] Wegh R T, Donker H and Meijerink A 1998 *Phys. Rev.* B **57** R2025
[32] Kirikova N Yu, Kirm M, Krupa J C, Makhov V N, Negodin E and Gesland J Y 2004 *J. Lumin.* **110** 135
[33] van Pieterson L, Reid M F, Wegh R T, Soverna S and Meijerink A 2002 *Phys. Rev.* B **65** 045113
[34] van Pieterson L, Reid M F, Wegh R T and Meijerink A 2001 *J. Lumin.* **94/95** 79
[35] van Pieterson L, Wegh R T, Meijerink A and Reid M F 2001 *J. Chem. Phys.* **115** 9382
[36] Reid M F, van Pieterson L, Wegh R T and Meijerink A 2000 *Phys. Rev.* B **62** 14744
[37] Kodama N, Yamaga M and Henderson B 1998 *J. Appl. Phys.* **84** 5820
[38] Burdick G W and Reid M F 2007 $4f^n$–$4f^{n-1}5d$ transitions *Handbook on the Physics and Chemistry of Rare Earths* vol 37, ed K A Gschneidner Jr, J-C G Bunzli and V K Pecharsky (Amsterdam: Elsevier) chapter 232
[39] Librantz A F H, Gomes L, Baldochi S L, Ranieri I M and Brito G E 2008 *J. Lumin.* **121** 137
[40] Collombet A, Guyot Y, Joubert M-F, Margerie J and Moncorgé R 2003 *Opt. Mater.* **24** 215
[41] Collombet A, Guyot Y, Joubert M F, Laroche M, Margerie J, Moncorgé R and Descroix E 2003 *Phys. Rev.* B **68** 035115
[42] Lo D, Makhov V N, Khaidukov N M, Krupa J C and Gesland J Y 2004 *J. Lumin.* **106** 15
[43] Guyot Y, Collombet A, Somatri T, Tkachuk A and Joubert M-F 2002 *J. Alloys Compounds* **341** 174
[44] Kirm M, Makhov V N, True M, Vielhauer S and Zimmerer G 2005 *Phys. Solid State* **47** 1416
[45] Kirm M, Stryganyuk G, Vielhauer S, Zimmerer G, Makhov V N, Malkin B Z, Solovyev O V, Abdulsabirov R Yu and Korableva S L 2007 *Phys. Rev.* B **75** 075111
[46] Wegh R T and Meijerink A 1999 *Phys. Rev.* B **60** 10820
[47] van Pieterson L, Reid M F and Meijerink A 2002 *Phys. Rev. Lett.* **88** 067405
[48] Chen Y, Kirm M, Negodin E, True M, Vielhauer S and Zimmerer G 2003 *Phys. Status Solidi* b **240** R1
[49] Makhov V N, Khaidukov N M, Kirikova N Yu, Kirm M, Krupa J C, Ouvarova T V and Zimmerer G 2000 *J. Lumin.* **87–89** 1005
[50] Khaidukov N M, Kirikova N Yu, Kirm M, Krupa J C, Makhov V N, Negodin E and Zimmerer G 2002 *Proc. SPIE* **4766** 154
[51] Makhov V N, Adamberg T, Kirm M, Vielhauer S and Stryganyuk G 2008 *J. Lumin.* **128** 725
[52] Oskam K D, Houtepen A J and Meijerink A 2002 *J. Lumin.* **97** 107
[53] Sarantopoulou E, Kobe S, Kollia Z, Podmiljsak B, McGuiness P J, Drazic G and Cefalas A C 2003 *J. Magn. Magn. Mater.* **267** 182
[54] van Pieterson L, Dullens R P A, Piejzel P S, Meijerink A and Jones G D 2001 *J. Chem. Phys.* **115** 9393
[55] Makhov V N, Batygov S Kh, Dmitruk L N, Kirm M, Stryganyuk G and Zimmerer G 2007 *Phys. Status Solidi* c **4** 881
[56] Makhov V N, Batygov S Kh, Dmitruk L N, Kirm M, Vielhauer S and Stryganyuk G 2008 *Phys. Solid State* **50** 1625
[57] Cefalas A C, Kobe S, Kollia Z and Sarantopoulou E 2002 *Cryst. Eng.* **5** 203

[58] Ivanovskikh K, Pustovarov V, Smirnov A and Shulgin B 2007 *Phys. Status Solidi* c **4** 889
[59] Ivanovskikh K, Pustovarov V, Smirnov A and Shulgin B 2008 *J. Alloys Compounds* **451** 65
[60] Ivanovskikh K V, Pustovarov V A, Kirm M and Shulgin B V 2007 *J. Lumin.* **122/123** 28
[61] Sarantopoulou E, Kollia Z, Cefalas A C, Semashko V V, Abdulsabirov R Yu, Naumov A K, Korableva S L, Szczurek T, Kobe S and McGuiness P J 2002 *Opt. Commun.* **208** 345
[62] Kirm M, Krupa J C, Makhov V N, True M, Vielhauer S and Zimmerer G 2004 *Phys. Rev.* B **70** 241101
[63] Yamaga M, Honda M, Kawamata N, Fujita T, Shimamura K and Fukuda T 2001 *J. Phys.: Condens. Matter* **13** 3461
[64] Kück S and Sokolska I 2006 *J. Phys.: Condens. Matter* **18** 5447
[65] Makhov V N, Khaidukov N M, Lo D, Kirm M and Zimmerer G 2003 *J. Lumin.* **102/103** 638
[66] Khaidukov N M, Kirm M, Lam S K, Lo D, Makhov V N and Zimmerer G 2000 *Opt. Commun.* **184** 183
[67] Khaidukov N M, Lam S K, Lo D, Makhov V N and Suetin N V 2002 *Opt. Mater.* **19** 365
[68] van der Kolk E, Dorenbos P, Kramer K, Biner D and Gudel H U 2008 *Phys. Rev.* B **77** 125110
[69] You F, Huang S, Liu S and Tao Y 2004 *J. Lumin.* **110** 95
[70] Sarantopoulou E, Cefalas A C, Dubinskii M A, Nicolaides C A, Abdulsabirov R Yu, Korableva S L, Naumov A K and Semashko V V 1994 *Opt. Lett.* **19** 499
[71] Stryganyuk G, Zimmerer G, Shiran N, Voronova V, Nesterkina N, Gektin A, Shimamura K, Villora E, Jing F, Shalapska T and Voloshinovskii A 2008 *J. Lumin.* **128** 1937
[72] Sarantopoulou E, Kollia Z, Cefalas A C, Semashko V V, Abdulsabirov R Yu, Naukov A K and Korableva S L 1998 *Opt. Commun.* **156** 101
[73] Makhov V N, Khaidukov N M, Kirm M, Zimmerer G, Lam S K, Lo D and Suetin N V 2002 *Surf. Rev. Lett.* **9** 271
[74] Alderighi D, Toci G, Vannini M, Parisi D, Bigotta S and Tonelli M 2006 *Appl. Phys.* B **83** 51
[75] Sarantopoulou E, Kollia Z and Cefalas A C 2000 *Opt. Commun.* **177** 377
[76] Kirm M, Chen Y, Neicheva S, Shimamura K, Shiran N, True M and Vielhauer S 2005 *Phys. Status Solidi* c **2** 418
[77] True M, Chen Y, Kirm M, Vielhauer S and Zimmerer G 2007 *J. Lumin.* **124** 279
[78] True M, Kirm M, Negodine E, Vielhauer S and Zimmerer G 2004 *J. Alloys Compounds* **374** 36
[79] Kirm M, Lichtenberg H, Makhov V N, Negodin E, Ouvarova T V, Suljoti E, True M and Zimmerer G 2002 *Radiat. Eff. Defects* **157** 911
[80] Van der Kolk E, Dorenbos P, van Eijk C W E, Vink A P, Fouassier C and Guillen F 2002 *J. Lumin.* **97** 212
[81] Gosowski M A and Ryba-Romanowski W 2008 *J. Phys. Chem.* C **112** 14196
[82] Yamaga M, Imai T, Miyairi H and Kodama N 2001 *J. Phys.: Condens. Matter* **13** 3461

[83] Barandiaran Z, Edelstein N M, Ordejon B, Ruiperez F and Seijo L 2005 *J. Solid State Chem.* **178** 464
[84] Reid M F, van Pieterson L and Meijerink A 2002 *J. Alloys Compounds* **344** 240
[85] Andriessen J, Van der Kolk E and Dorenbos P 2007 *Phys. Rev.* B **76** 075124
[86] Meyer G 1982 *Prog. Solid State Chem.* **14** 141
[87] Bucher E, Guggenheim H J, Andres K, Hull G W and Cooper A S 1974 *Phys. Rev.* B **10** 2945
[88] Tanner P A 2004 *Top. Curr. Chem.* **241** 167
[89] Tanner P A, Ning L, Makhov V N, Khaidukov N M and Kirm M 2006 *J. Phys. Chem.* B **110** 12113
[90] Tanner P A, Liu Y-L, Edelstein N, Murdoch K and Khaidukov N M 1997 *J. Phys.: Condens. Matter* **9** 7817
[91] Thorne J R G, Jones M, McCaw C S, Murdoch K M, Denning R G and Khaidukov N M 1999 *J. Phys.: Condens. Matter* **11** 7851
[92] Berry A J, Morrison I D and Denning R G 1998 *Mol. Phys.* **93** 1
[93] Zhou X-J, Tanner P A and Faucher M D 2007 *J. Phys. Chem.* C **111** 683
[94] Tanner P A and Faucher M D 2007 *Chem. Phys. Lett.* **445** 183
[95] Falin M L, Gerasimov K I, Leushin A M and Khaidukov N M 2008 *J. Lumin.* **128** 1103
[96] Zhou X, Reid M F, Faucher M D and Tanner P A 2006 *J. Phys. Chem.* B **110** 14939
[97] Aull B F and Jenssen H P 1986 *Phys. Rev.* B **34** 6640
[98] Aull B F and Jenssen H P 1986 *Phys. Rev.* B **34** 6647
[99] Bunuel M A, Moine B, Jacquier B, Garcia A and Chaminade J P 1999 *J. Appl. Phys.* **86** 5045
[100] Schiffbauer D, Wickleder C, Meyer G, Kirm M, Stephan M and Schmidt P C 2005 *Z. Anorg. Allg. Chem.* **631** 3046
[101] Bunuel M A, Lozano L, Chaminade J P, Moine B and Jacquier B 1999 *Opt. Mater.* **13** 211
[102] Makhov V N, Khaidukov N M, Lo D, Krupa J C, Kirm M and Negodin E 2005 *Opt. Mater.* **27** 1131
[103] Ma C, Tanner P A, Xia S and Yin M 2007 *Opt. Mater.* **29** 1620
[104] Zimmerer G 2007 *Rad. Meas.* **42** 859
[105] Tanner P A, Ravi Kanth Kumar V V, Jayasankar C K and Reid M F 1994 *J. Alloys Compounds* **215** 349
[106] Duan C K and Tanner P A 2008 *J. Phys.: Condens. Matter* **20** 215228
[107] Dorenbos P 2000 *J. Lumin.* **91** 91
[108] Dorenbos P 2003 *J. Phys.: Condens. Matter* **15** 8417
[109] Li L and Zhang S Y 2006 *J. Phys. Chem.* B **110** 21438
[110] Ning L, Mak C S K and Tanner P A 2005 *Phys. Rev.* B **72** 085127
[111] Kuze S, du Boulay D, Ishizawa N, Kodama N, Yamaga M and Henderson B 2004 *J. Solid State Chem.* **177** 3505
[112] Duan C K and Reid M F 2003 *J. Solid State Chem.* **171** 299
[113] Ning L X, Duan C K, Xia S D, Reid M F and Tanner P A 2004 *J. Alloys Compounds* **366** 34
[114] Xia S D, Duan C K, Deng Q and Ruan G 2005 *J. Solid State Chem.* **178** 2643